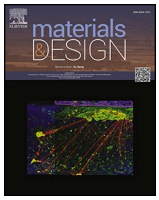
Materials & Design 258 (2025) 114687



Contents lists available at ScienceDirect

Materials & Design

journal homepage: www.elsevier.com/locate/matdes



A simple putty to enable the shaping of silica glass

Iuliia S. Tirichenko [a,*], Yinglun Hong [b], Christopher Butler [b], Eduardo Saiz [b]

[a] Department of Mechanical Engineering, Imperial College London, London SW7 2AZ, UK
[b] Department of Materials, Imperial College London, London SW7 2AZ, UK

ARTICLE INFO

Keywords:
Glass
Additive manufacturing
3D-printing
Shaping
Forming

ABSTRACT

Glass has been used for centuries, and its compositions and applications are continuously evolving. Advancements in glass shaping are being made from micro to macro scales. However, robust fabrication of increasingly complex glass parts remains a significant challenge in industrial applications which also demand more sustainable manufacturing processes. Novel additive manufacturing technologies could offer useful alternatives, but working with glass has proven complex. We have created a "glass putty" composed of micron-sized glass powder and resin that can be shaped at room temperature by 3D printing, plasticine-like moulding, stamping, and green machining. Our approach enables multiscale, high-quality transparent glass components with properties comparable to commercial materials while reducing manufacturing hazards. The adhesive nature of the putty allows its modular assembly to produce colour gradients. The putty can be reshaped in case of errors, reducing the part rejection rate. Such a multiscale and multitool forming approach to glass manufacturing unlocks the true freedom of design when working with this challenging material and will help to realise its true potential in any desired application.

1. Introduction

Glass is omnipresent in our daily lives, from bottles on our tables and displays in our phones to complex microfluidic devices in hospital laboratories. Despite the long history, the fundamental glass-making process remains largely unchanged since its discovery. With the rise of new applications there is a demand for glass parts with increasingly complex designs and new techniques have been developed to meet this demand. Additive manufacturing is at the forefront of these developments. Methods such as molten glass extrusion, lithography, stereolithography, robocasting and laser powder bed fusion were shown to be able to manufacture high-quality glass [1–11]. While highly promising, these techniques often require a high degree of control, the use of hazardous chemicals and nano-powders or complex post-processing. Moreover, additive manufacturing requires specialised equipment and suspensions that often have complex formulations involving nanopowders and multiple organic components. Therefore, 3D printing remains a cost-heavy option for most industries that tend to rely on traditional techniques such as blowing, stamping, and cutting. Those techniques, while cheap and well-developed, still have high rejection rates and are limited in achievable shapes. There is thus a strong need for a technology that will either have a low adoption barrier or provide tools to leverage existing equipment, thereby increasing sustainability and minimising costs.

Here we present a widely versatile hybrid method of room temperature glass free-shaping. The method is based on the formulation of a malleable glass-polymer composite that can be easily machined, shaped by hand or extruded. The composite consists of just three components – silica powder, phenolic resin and ethanol. The phenolic resin acts as a triple-functional building block – a dispersion medium, a curable binder, and a plasticiser. The silica powder is in the form of microscopic particles (<63 μm), and forms up to 53.5 vol% paste in a highly viscous ethanol-phenolic resin mix, where the former serves as a fast-drying solvent. The composite can be shaped by cutting, sculpting, stamping and machining. It can also be 3D printed using robocasting into standalone items and pre-forms that can be further shaped post-extrusion enabling complex bulk and surface designs. The composite is designed for room temperature shaping, easily preserving created structures by air drying. Its simple formulation is adaptable to multiple technologies including additive manufacturing. The parts can then be debinded and fired above the melting point of silica to densify and form an optically transparent glass. Unlike other silica sintering techniques that rely on the combination of nanopowders with carefully adjusted sintering schedules, firing above the melting point enables fast sintering and

* Corresponding author.
E-mail address: i.elizarova14@imperial.ac.uk (I.S. Tirichenko).

https://doi.org/10.1016/j.matdes.2025.114687
Received 6 May 2025; Received in revised form 14 August 2025; Accepted 2 September 2025
Available online 2 September 2025
0264-1275/© 2025 The Authors. Published by Elsevier Ltd. This is an open access article under the CC BY license (http://creativecommons.org/licenses/by/4.0/).

healing of small defects formed during shaping even though it may limit the ability to implement very fine design details. The use of micro-sized silica powder provides a significant advantage as it reduces health risks associated with the more commonly used nano-powders. Additionally, it reduces manufacturing costs and paves the way for easier glass recycling, as breaking glass down to micron-sized particles is less energy-intensive. The high viscosity of molten silica enables thermal finishing that produces transparent glass with exceptional precision to the original design, even in complex shapes, with minimal to no distortion.

2. Results and discussion

2.1. Paste flow properties and extrusion behaviour

After mixing the components, the paste is used to print dense pre-forms layer by layer using extrusion through a microscopic nozzle. The extrusion process itself is critical in preventing large bubble defects because although the pastes undergo defoaming, some residual air remains trapped due to their high viscosity, which is then released during extrusion. This creates small gaps between the paste lines being printed, that are filled in by the subsequent paste layers, and are further eliminated during re-melting to produce high quality glass. The paste can also be used for the direct 3D printing of finer mouldable objects using robocasting. The process relies on a smooth extrusion process and on the part retaining its shape after printing. The paste thus must exhibit shear-thinning behaviour, reducing its viscosity under applied stress. Rheological measurements of the optimised ink reveal favourable flow behaviour for the process (Fig. 1). It is evident that the viscosity adheres to the desirable trend and the ink exhibits shear-thinning properties. The shear-thinning coefficient for this ink is $n = 0.45$ as derived from the graph Fig. 1a and the power law fitting

$$\eta = K\dot{\gamma}^{n-1} \tag{1}$$

where η is the viscosity, K is the consistency index, $\dot{\gamma}$ is the strain rate, and n is the shear thinning coefficient (power law constant). The power law fitting has been chosen to describe the viscosity of the inks instead of a more commonly used Herschel-Bulkley model. When applied to the intermediate shear range, i.e. in conditions of stable flow, the power law fitting provides a more accurate estimate of the shear thinning coefficient. This is due pseudoplastic behaviour of the ink being challenging to accurately measure at low and high shear [12]. The coefficient quantifies the extent of non-Newtonian flow behaviour, with smaller n values indicating a greater shear-thinning character.

The stress at which the ink starts to flow, the flow point $\tau_\gamma = 48.3Pa$, can be found on the intersection of the graphs for storage and loss moduli depicted in Fig. 1b. This indicates relatively low extrusion pressures required for printing. The extrusion pressure experiment (Fig. 1c) confirms the finding – the pressure required to initiate the flow from a ∅ 9.54 mm syringe was found to be 2.24 *MPa*. It is worth noting that the pressure required to initiate the flow is significantly higher than the stable flow pressure of 0.83 *MPa*. Furthermore, the flow termination is not immediate. The ink continues to flow for several minutes after the piston comes to a stop. To prevent printing defects, 3D models should feature appropriate lead-ins and lead-outs so that the print falls within the "stable flow" pressure range.

2.2. Multiscale shaping capabilities

After extrusion the pre-forms can be further shaped using either wet or dry methods (Fig. 2). The size of the pre-forms ranges from 0.6 mm to 1.5 cm in height, reaching 5 cm in x-y dimensions. Wet shaping includes clay-like forming, cutting, and stamping, and requires the pre-forms to be at optimum workable condition. Such a condition is achieved when the print is easily mouldable without breaking, keeps the shape once moulded and is not sticky to the touch. It is determined by the amount of solvent remaining in the print which decreases with drying time. Thin prints ranging from sub-mm to 2 mm can be moulded (Fig. 2a) within 1–4 h of bench room temperature drying. Thicker pre-forms of 3 to 5 mm require longer drying times, from 24 to 72 h, after which they can be shaped for up to 12 more hours. Once shaped, parts maintain the design and can be left to air-dry to reach full hardness.

For stamping (Fig. 2b, c), it is necessary to wait for the formation of a thin dried layer of solidified phenolic resin on top of the print. This prevents the stamp from sticking and helps the retention of the created impression. The layer forms within minutes post-extrusion. The achievable stamp resolution is ~0.1 mm (Fig. 2c, 4d). Small stamping features require a softer state of the printed pre-form, while larger patterns can be manufactured up to several hours before the complete drying of the part.

To shape by machining, the pre-form (Fig. 2d) must be dried and cured at 165 °C, the curing temperature of the phenolic resin. Once treated, it can be effortlessly machined using standard carbide CNC or hand tools, ground and polished if necessary. During machining the surface of the pre-form might become burnt due to poor dissipation of heat. This, however, does not appear to compromise the quality of the final product.

The method also offers the capability to produce composites in a modular manner. Once extruded, the parts can be joined together much like sticking plasticine pieces as the inks are adhesive. This can be used to create, for example, internal structures in glass by placing sacrificial structures between two printed pre-forms (Fig. 2e). The bottom pre-form is printed first, followed by placing a plastic microchannel negative shape on top. It is then placed back inside the printer, where the top part is printed directly onto it. The composite is left to fully dry before further thermal processing. The modular capability can also be used to create

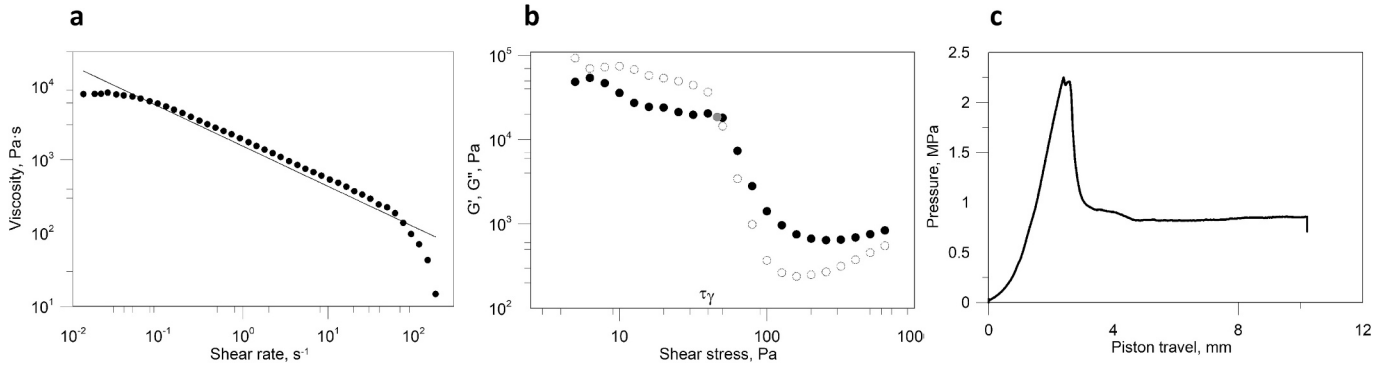


Fig. 1. Rheological properties of the SiO2-phenolic resin ink. (a) The flow ramp demonstrating shear-thinning behaviour, (b) dynamic strain sweep indicating the flow point of the ink $\tau_\gamma = 48.3Pa$, (c) extrusion test showing the pressure = 2.24 MPa is required to start the flow of the ink from a ∅9.54 syringe through a ∅0.61 mm conical nozzle (printing configuration).

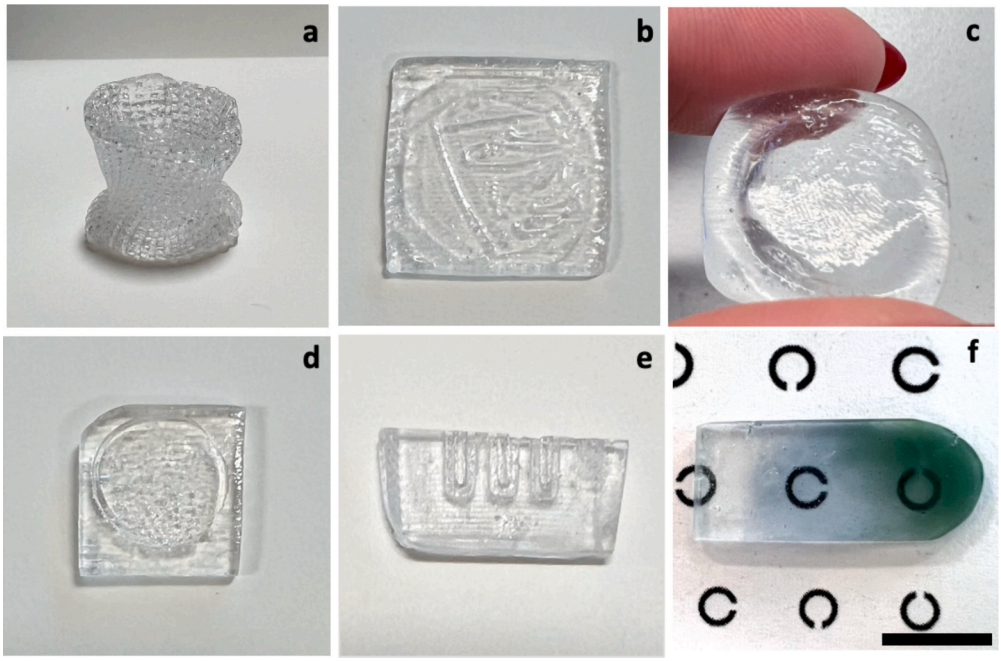


Fig. 2. Showcase of the technological capabilities. (a) Complex perforated artefact moulded by hand from a direct ink writing printed flat thin net; (b) printed pre-form that is stamped with a coin; (c) printed pre-form that is stamped with a fingerprint to capture micron-sized features; (d) a well shape obtained by machining a printed pre-form; (e) microchannels obtained by using sacrificial templates; (d) modular-assembled colour (Cr_2O_3) gradient glass piece. The scale bar is 1 cm.

coloured glasses with gradients with possible applications in gradient-index optics. The colouring of the glass is achieved by the addition of metal oxides into the pastes, as illustrated by the Cr_2O_3 example (Fig. 2f). Using three pastes with different pigment loading (0, 0.15, and 0.2 wt% of silica powder), three pre-forms were extruded and put together by hand. The pigments used in this system must be stable at high temperatures both in air and in vacuum to withstand the thermal treatment. Metallic nanoparticles and quantum dots, for example, cannot be used as they will degrade at the temperatures above 1700 °C required to melt the glass. The chosen oxide colourants must not reduce during vacuum heat treatment; oxides with low oxidation potentials, such as copper or iron, can revert to their metallic state. Introduction of any pigments into the glass melt will generally decrease its viscosity; the amount of pigment added must be thus minimised to avoid significant viscosity decrease as this could affect shape retention during firing and promote crystallisation during cooling.

2.3. Melting of pre-forms into pure transparent glass

The primary advantage of our method is precise shaping at room temperature. The parts, however, must be still heat-treated to achieve transparency. A slow burnout at 600 °C is required to remove the resin, followed by a swift ramp to partial sintering at 1600 °C for 2 h and 2-minute remelting at 1780 °C for 2 min in a high vacuum. The finished dense parts exhibit final shrinkage of 7.5 % to an original design (measured on a standard rectangular bar print).

The initial sintering and further densification processes are rapid. The time required to form a 100 nm neck between micron sized particles is ~ 10^{-2} s, defined by the equation [13]:

$$\left(\frac{X}{D}\right)^2 = \frac{3\gamma t}{2\eta D} \tag{2}$$

where η is the viscosity of the material ($7{\cdot}10^5$ Pa·s at 1800°C [14]), D is particle diameter (1 μm), X is the size of the neck between particles, γ is surface energy (~0.3 J/m^2 [15]). The time to reach full densification (from 50 %, state of the green pre-form) can be derived from

$$\left(\frac{\gamma}{\eta l_0}\right)\left(\frac{\rho_s}{\rho_0}\right)^{\frac{1}{3}}(t - t_0)\ 2.5 \tag{3}$$

where, l_0 is initial cell dimension (order of particle size), ρ_o is initial density, ρ_s is final density, t is time of the densification process and t_0 a fictitious time at which the density is zero. The proportionality coefficient 2.5 is extracted from a graph of the Scherer's glass densification model [16]. The time to reach full densification of silica glass ($\frac{\rho_s}{\rho_0} = 1$, from the starting point of $\rho_0 = 0.5\rho_s$) is then calculated to be ~ 5 s. Thus, the firing process to achieve full density glass is the order of seconds.

For centimeter sized parts the associated Bond number, $\frac{\rho g L^2}{\gamma}$, where g is the gravitational acceleration and L is a characteristic length scale (of the order of the part size) is larger than one. This suggests that gravitational forces are dominant over capillary ones. To give an idea of the speed of deformation under gravitational forces, we can compare the times required for sintering with the times required for bending a viscous beam clamped in one side due to gravity. This is an estimation of the expected degree of sagging for an overhang feature. The characteristic velocity, W, for the initial bending of a beam with length L and thickness H will be [17]:

$$W = \frac{g\delta\rho L^4}{\eta H^2} \tag{4}$$

where $\delta\rho$ is the difference in density between the glass and the atmosphere (~2.1 g/cm^3). For an overhang formed by a plate with a length of 0.5 cm and a thickness of 1 mm, W ~ 20 μm/s. This means that in the sintering times of few seconds calculated above, the degree of bending will be well below the thickness of the plate. For small features distortion may be driven by capillary forces that try to minimize the surface energy. We can estimate the speed of capillary driven change using as a reference the speed of glass spreading (also driven by capillarity) [18]. The maximum expected speeds for molten silica glass drops on inert substrates are of the order of 1 μm/s – small compared with the calculated sintering times. Our results suggest that we can retain details with characteristics sizes in the order of 100 s of microns without major

distortion.

Close to the melting point, the viscosity of the silica melt [19] ranges between 10^5-10^6 Pa·s, which is sufficient to preserve the details and high aspect ratio features of the pre-forms without significant distortion. While helping to preserve the shape, the high viscosity hinders the removal of trapped air, which can reduce transparency and compromise properties. The velocity of a spherical bubble leaving a viscous liquid cast described by the Hadamard-Rybczynski equation [20]

$$v = \frac{2r^2 g(\rho_b - \rho)}{3\eta}\beta \tag{5}$$

where v is the steady-state velocity of a bubble radius r, , ρ_b is the density of the bubble, ρ is the density of the liquid, and $\beta = (1+\kappa)/(2+3\kappa)$ and $\kappa = \eta_b/\eta$ with η_b the viscosity of the bubble phase. Thus, to calculate the velocity of a CO_2 bubble escaping silica melt at 1780 °C, we take the viscosity of glass at that temperature, assuming bubble size range of 10 – 100 μm, and find the value of v~•10^{-13}-•10^{-11} m/s. Such low mobility of gas bubbles prevents their easy removal during the short heating cycle required to preserve the shape of the pre-form. To minimise this, the key step of extrusion, as well as firing in a vacuum, must be performed regardless of the shaping method chosen.

The resulting glass exhibits ultra-violet and visible transparency of the range similar to a commercial microscope glass slide (Fig. 3a). The chemical nature of the glass is confirmed to be pure fused silica by Raman spectroscopy (Fig. 3b) and X-ray photoelectron spectroscopy (Fig. 3c). Slight differences in the Raman spectra of the printed and commercial glass may result from the formation of small amounts of residual cristobalite during cooling (supplementary Fig. 6). No crystalline phase can be found by XRD (Fig. S4) and the trace cristobalite does not appear to have a significant effect on the final glass properties. The mean elastic modulus of the printed glass was measured using nano-indentation (Fig. 3e, supplementary Fig. 1) is 59.91 GPa. Reported modulus values for fused silica are in range of 60–72 GPa[21,22]. Supplementary Fig. 4 shows that the material is amorphous as further validated by X-ray diffraction analysis. The average surface profile roughness of the as printed material is 3.7 μm (supplementary Fig. 7).

Overall, we have used our approach to produce bubble-free parts in the centimetre scale. Even when firing in vacuum and using the pre-extrusion step thicker walls may hamper the elimination of trapped bubbles. Larger thin-walled items might be produced with no detriment to transparency; there is some limitation in the complexity of the designs as gravity will increasingly affect the stability of large overhanging features. The main implication for scale-up is the need to balance the melting conditions: the parts must be kept above the melting point long enough for viscous sintering and pore elimination but not too long as to preserve the geometry. Although re-melting during sintering will close bubbles and small drying cracks, scaling up should also require an optimization of the drying conditions as to avoid the formation of large defects.

One of the advantages of this method is the possibility of recycling the glass putty. Defective putty can be fixed if the mixture is fresh; if required the powder content can be increased and re-mixed. If the powder content in the putty is too large, the issue is more difficult to fix, as adding solvent to the mixture thins out the resin and reduces malleability. The putty is difficult to reuse once it is dry, as significant amount of solvent is needed to re-dissolve the resin, resulting in a low-viscosity putty that does not print or holds shape.

3. Conclusions

In summary, we have developed a simple tricomponent “glass putty” that can be 3D printed, cut, stamped or machined, allowing for ultimate optionality in the manufacturing approach. The formulation uses micron-sized silica particles that can be easily obtained by grinding recycled glass. It produces transparent high-quality glass parts regardless of the shaping method, with exceptional precision using additive or subtractive manufacturing. It helps to broaden the design space of glass components by enabling the implementation of complex shapes and the spatial manipulation of optical properties. This advance highlights the need to adopt innovative ways to manufacture glass, promoting accessibility across various applications.

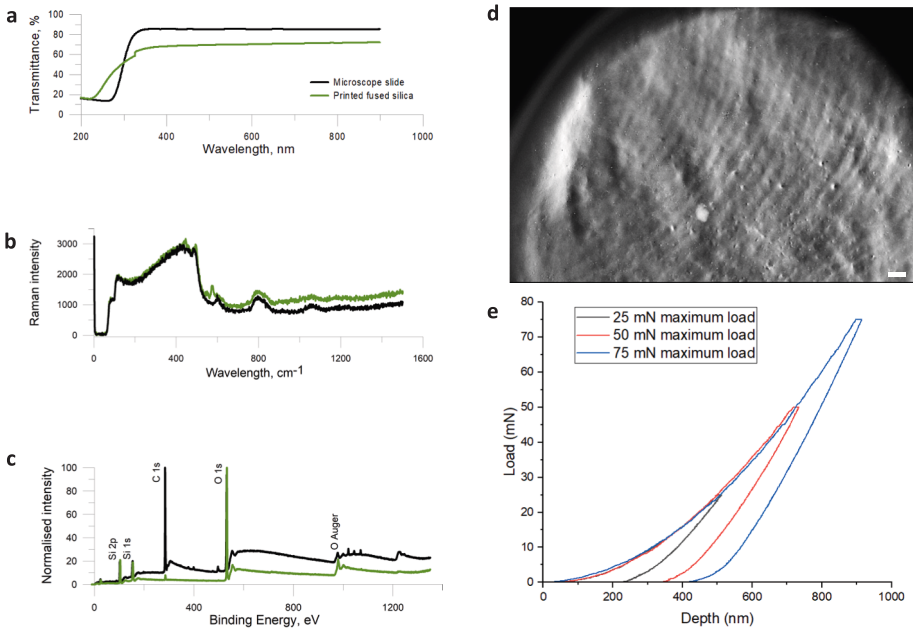


Fig. 3. Properties of the shaped glass. (a) UV–VIS transparency measurement indicating ~10 % difference with a commercial glass slide in visible spectrum, (b) Raman spectra and (c) XPS spectra confirming the purity of the shaped glass (compared to commercial fused SiO2), (d) SEM image of the fingerprint on glass indicating micron resolution of stamping on printed pre-forms (scale bar 500 μm), (e) Examples of load versus nanoindenter displacement curves for calculation of elastic modulus.

4. Methods

Materials. White quartz silica powder and chromium oxide powder (Cr_2O_3 the colourant) were purchased from Sigma Aldrich, Germany. Low free phenol content phenolic resin Durez 30,562 was kindly provided by Sumimoto Bakelite Europe, Belgium. Ethanol was purchased from VWR International.

Paste preparation. Phenolic resin was dissolved in ethanol to form 66.7 wt% solution at 37 °C overnight. Silica powder was dispersed in the phenolic resin solution using a planetary mixer (ARE-250, Thinky, Japan) at 2000 rpm for 30 s, repeated 4 times with cooling steps to form a 50 vol% ink. It was then de-foamed at 2200 rpm for 5 min and loaded into 3 ml printing syringe barrels (Nordson).

Colouring. 0.1 and 0.2 wt% Cr_2O_3 powder were added to the stock silica powder via ball milling. The mixed powder was then used to fabricate pastes as above.

3D-printing. All samples were printed using 3dInks direct ink writing system (USA) at 15 mm/s with a conical ∅0.61 mm nozzle (Nordson) onto flat paper substrates greased with oleomargarine. The samples were then subject to drying (from 1 h to 4 days, depending on the geometry and size) and post-printing shaping.

Shaping. The printed parts were further formed using several techniques. *Hand-shaping* was used to create thin-walled structures with unsupported and high-aspect ratio features. The printed nets were separated from the substrate paper after 1 h of drying and shaped by hand with no visible damage to the prints. *Stamping* was performed on 30x30x3 mm square prints. After 2 h of drying, the stamps (coin, finger) were pushed into the prints and removed immediately. For machining, the parts were printed, dried for 4 days, and then cured at 165 °C for 10 min. The Roland MDX-40A CNC machine with a tungsten carbide drill was used to drill out the circle pattern.

Thermal treatment. The parts were heated at 1 °C/min to 600 °C in air to slowly burn out the phenolic resin binder. They were then sintered at 1600 °C in air for 2 h. The sintered parts were melted in high-temperature vacuum furnace at 1780 °C and 10^{-5} vacuum for 2 min. Step-by-step results of thermal treatment, as well as some of associated challenges, are available in Fig. S1.

Paste characterisation. Rheology experiments were performed using a 40 mm parallel plate geometry (Discovery HR-1, TA Instruments, Germany) at 25 °C. The storage and loss moduli of the paste were obtained using oscillating torque experiments. A strain rate ramp experiment was conducted to evaluate the shear thinning behaviour. Extrusion pressure was assessed using a push test. 3 ml printing syringes, ∅0.61 mm nozzles, ∅9.54 mm robocasting piston and Zwick/Roell Z010 mechanical tester as a controlled pressure source were used to move the piston at the displacement rate 1.2 mm/min to obtain the plateau pressure value (stable extrusion).

Powder and glass characterisation. Scanning electron microscopy (JEOL 6100, 20 kV) was used to assess the quality of the patterns and the morphology of the raw silica powder (Fig. S2). Particle size for the silica powder was confirmed using Mastersizer 2000 laser diffraction particle size analyser from Malvern Panalytical (Fig. S3). X-ray powder diffraction (D2 Phaser, Bruker) was used to ensure the amorphous nature of the printed glass (Fig. S4). X-ray photoelectron spectroscopy (K-Alpha+, Thermo Scientific) and Raman spectroscopy (inVia Raman Microscope, Renishaw) was used to confirm the purity of the printed silica glass. Transparency of the glass was characterised using ultraviolet–visible spectroscopy (Perkin Elmer Lambda 25). Surface profile roughness was measured using Olympus Lext 3D measuring laser microscope OLS5000.

Elastic modulus was measured using nanoindentation experiment. Indents were performed on one sample, hot-mounted in Bakerlite and polished to 6 μm surface finish. Each indent was performed via a MicroMaterials NanoTest Vantage platform 5 nanoindenter. All indents we carried out with a Berkovich indenter. To avoid cracking on indentation, cycles with low maximum loads of 25mN, 50 mN and 75 mN were used. 20 indents in a row were applied at each load, with loading/unloading rates of 0.5 mN/s, 1 mN/s and 1.5 mN/s respectively. A 60 s dwell period is applied at maximum load, to ensure that time dependent plastic effects within the fused silica are reduced. A 30 s thermal drift correction period is applied post indentation at appoint 80 % through the unload cycle. Each indent was offset with 10 μm from the last, and each row was offset by 15 μm. The depth versus load curves for all accepted indentation cycles are presented in Fig. S5.

Unloading stiffness and hardness for each indent was calculated via P5 NanoTest Vantage software. Firstly, indentation cycles which are affected by surface roughness and porosities are removed. A power law fit is applied to the unloading curve (Oliver and Pharr method), fitting through 100 % to 20 % of the maximum load with post indentation thermal drift correction. A diamond area function calibration (on fused silica) corrects for variance in the Berkovich tip profile. The elastic modulus (E_s) can be calculated from the reduced modulus (E_r) through:

$$\frac{1}{E_r} = \frac{(1-\nu_s^2)}{E_s} + \frac{(1-\nu_i^2)}{E_i} \tag{6}$$

where the Poisson's ratio for the diamond indenter (ν_i) is 0.07 and for the sample (ν_s) is 0.17. The elastic modulus of the indenter (E_i) is 1141 GPa.

CRediT authorship contribution statement

Iuliia S. Tirichenko: Writing – review & editing, Writing – original draft, Supervision, Methodology, Investigation, Formal analysis, Data curation, Conceptualization. **Yinglun Hong:** Investigation. **Christopher Butler:** Investigation, Formal analysis. **Eduardo Saiz:** Writing – review & editing, Resources, Methodology, Investigation, Funding acquisition, Conceptualization.

Funding

This work was supported by the EPSRC Program Manufacture Using Advanced Powder Processes (MAPP) EP/P006566/1.

Declaration of competing interest

The authors declare that they have no known competing financial interests or personal relationships that could have appeared to influence the work reported in this paper.

Acknowledgments

During the preparation of this work the authors used ChatGPT 40 in order to aid editing the writing style of the manuscript. After using this tool/service, the authors reviewed and edited the content as needed and take full responsibility for the content of the published article.

Appendix A. Supplementary data

Supplementary data to this article can be found online at https://doi.org/10.1016/j.matdes.2025.114687.

Data availability

Data will be made available on request.

References

[1] D.T. Nguyen, C. Meyers, T.D. Yee, N.A. Dudukovic, J.F. Destino, C. Zhu, E.B. Duoss, T.F. Baumann, T. Suratwala, J.E. Smay, R. Dylla-Spears, 3D-printed transparent glass, Adv. Mater. 29 (2017) 1701181, https://doi.org/10.1002/adma.201701181.
[2] J. Klein, M. Stern, G. Franchin, M. Kayser, C. Inamura, S. Dave, J.C. Weaver, P. Houk, P. Colombo, M. Yang, N. Oxman, Additive manufacturing of optically transparent glass, And Addit. Manuf. 2 (2015) 92–105, https://doi.org/10.1089/3dp.2015.0021.

[3] M. Mader, O. Schlatter, B. Heck, A. Warmbold, A. Dorn, H. Zappe, P. Risch, D. Helmer, F. Kotz, B.E. Rapp, High-throughput injection molding of transparent fused silica glass, Science 372 (2021) 182–186, https://doi.org/10.1126/science.abf1537.
[4] F. Kotz, K. Arnold, W. Bauer, D. Schild, N. Keller, K. Sachsenheimer, T.M. Nargang, C. Richter, D. Helmer, B.E. Rapp, Three-dimensional printing of transparent fused silica glass, Nat 544 (2017) 337–339, https://doi.org/10.1038/nature22061.
[5] O. Yong-Taeg, S. Fujino, K. Morinag, Fabrication of transparent silica glass by powder sintering, Sci. Technol. Adv. Mater. 3 (2002) 297–301, https://doi.org/10.1016/S1468-6996(02)00030-X.
[6] J.T. Toombs, M. Luitz, C.C. Cook, S. Jenne, C.C. Li, B.E. Rapp, F. Kotz-Helmer, H. K. Taylor, Volumetric additive manufacturing of silica glass with microscale computed axial lithography, Science 376 (2022) 308–312, https://doi.org/10.1126/science.abm6459.
[7] R. Dylla-Spears, T.D. Yee, K. Sasan, D.T. Nguyen, N.A. Dudukovic, J.M. Ortega, M. A. Johnson, O.D. Herrera, F.J. Ryerson, L.L. Wong, 3D printed gradient index glass optics, Sci. Adv. 6 (2020) eabc7429, https://doi.org/10.1126/sciadv.abc7429.
[8] D. Zhang, X. Liu, J. Qiu, 3D printing of glass by additive manufacturing techniques: a review, Front. Optoelectron. 14 (2021) 263–277, https://doi.org/10.1007/s12200-020-1009-z.
[9] P. Cai, L. Guo, H. Wang, J. Li, J. Li, Y. Qiu, Q. Zhang, Q. Lue, Effects of slurry mixing methods and solid loading on 3D printed silica glass parts based on DLP stereolithography, Ceram. Int. 46 (2020) 16833–16841, https://doi.org/10.1016/j.ceramint.2020.03.260.
[10] Y. Xu, Y. Li, N. Zheng, Q. Zhao, T. Xie, Transparent origami glass, Nat. Commun. 12 (2021) 4261, https://doi.org/10.1038/s41467-021-24559-x.
[11] Z. Hong, P. Ye, D.A. Loy, R. Liang, Three-dimensional printing of glass micro-optics, Optica 8 (2021) 904, https://doi.org/10.1364/OPTICA.422955.
[12] V.G. Rocha, E. Saiz, I.S. Tirichenko, E. García-Tuñón, Direct ink writing advances in multi-material structures for a sustainable future, J. Mater. Chem. A 8 (2020) 15646–15657, https://doi.org/10.1039/D0TA04181E.
[13] M.W. Barsoum, Fundamentals of Ceramics, 2nd ed.,, CRC Press, 2019 doi: 10.1201/9781498708166.
[14] J.D. Musgraves, J. Hu, L. Calvez (Eds.), Springer Handbook of Glass, Springer International Publishing, Cham, 2019 doi: 10.1007/978-3-319-93728-1.
[15] W.D. Kingery, Surface tension of some liquid oxides and their temperature coefficients, J. Am. Ceram. Soc. 42 (1959) 6–10, https://doi.org/10.1111/j.1151-2916.1959.tb09134.x.
[16] G.W. Scherer, D.L. Bachman, Sintering of low-density glasses: II, experimental study, J. Am. Ceram. Soc. 60 (1977) 239–243, https://doi.org/10.1111/j.1151-2916.1977.tb14115.x.
[17] N.M. Ribe, Bending and stretching of thin viscous sheets, J. Fluid Mech. 433 (2001) 135–160, https://doi.org/10.1017/S0022112000003360.
[18] S. Lopez-Esteban, E. Saiz, J.S. Moya, A.P. Tomsia, Spreading of viscous liquids at high temperature: silicate glasses on molybdenum, Langmuir 21 (2005) 2438–2446, https://doi.org/10.1021/la0474621.
[19] G. Urbain, Y. Bottinga, P. Richet, Viscosity of liquid silica, silicates and alumino-silicates, Geochimica et COsmochimica Acta 46 (1982) 1061–1072, https://doi.org/10.1016/0016-7037(82)90059-X.
[20] L.E. Jackson, F.B. Wadsworth, J. Mitchell, C. Rennie, E.W. Llewellin, K. Hess, D. B. Dingwell, Bubble rise in molten glasses and silicate melts during heating and cooling cycles, J. Am. Ceram. Soc. 105 (2022) 7238–7253, https://doi.org/10.1111/jace.18680.
[21] L. Zheng, A.W. Schmid, J.C. Lambropoulos, Surface effects on Young's modulus and hardness of fused silica by nanoindentation study, J. Mater. Sci. 42 (2007) 191–198, https://doi.org/10.1007/s10853-006-1051-2.
[22] F. Dahmani, J.C. Lambropoulos, A.W. Schmid, S.J. Burns, C. Pratt, Nanoindentation technique for measuring residual stress field around a laser-induced crack in fused silica, J. Mater. Sci. 33 (1998) 4677–4685, https://doi.org/10.1023/A:1004424717548.